Stabilization Mechanism and Multi-field Coupling Effect of High Steep Loess Slope under Heavy Rainfall

Jinggang Liu, Yaoxian Xie, Jiangtao Liu, Xian Zhao, Xianwen Huang, Daheng Peng

Abstract—**The instability of high and steep loess slopes under intense rainfall poses a major threat to infrastructure in loess regions. This study combines indoor model tests and numerical simulations to systematically analyze the evolution of the seepage field, pore water pressure response, displacement distribution, and failure modes during rainfall infiltration. Results show that slope instability follows a four-stage process: rainfall infiltration initiates the downward movement of the wetting front and dual seepage paths, leading to crack development at the crest and stress concentration at the toe; pore water pressure exhibits a dynamic "double-peak and double-drop" pattern, with abrupt drops caused by crack penetration being a key trigger of landslides; continued degradation of shallow soil strength ultimately leads to overall instability. Displacement monitoring indicates that sliding mainly occurs within the shallow layer, with a maximum vertical displacement of 4.2 cm forming a curved sliding surface within 0.3 m. Numerical simulations validate the coupled seepage-stress-displacement mechanism, yielding a safety factor of 0.705. The findings suggest that drainage channels and reinforcement techniques should be implemented to control pore pressure and improve slope stability, providing valuable reference for similar engineering applications.**

Index Terms—**Heavy rainfall; Steep loess slope; Laboratory model tests; Numerical simulation; Instability mechanism**

I. Introduction

THE instability of high and steep loess slopes induced by intense rainfall is a typical geological disaster in loess areas, characterized by strong suddenness and great destructiveness, posing a severe threat to infrastructure and public safety [1]. Due to its large pores, strong permeability, and weak erosion resistance [2]-[3], loess is prone to progressive failures such as shallow sliding under intense rainfall. Additionally, steep slope terrain can further amplify these risks. With global climate change, extreme rainfall events in the northwest region have become more frequent [5], leading to increasingly severe issues of instability in high and steep slopes. Therefore, systematically exploring the water migration patterns in slope soil and the evolution mechanism of its stability under rainfall conditions has significant academic and engineering application value.

In recent years, indoor model tests and numerical simulation techniques have made significant progress in revealing the mechanisms of slope instability induced by rainfall. Studies have shown that the coupling effects of rainfall patterns, seepage boundary conditions, and soil characteristics jointly control the process of slope instability [6]. In terms of indoor experiments, Zhu Jiandong et al. [7] found through comparative tests that soil loss caused by intermittent rainfall increased by 43% compared to continuous rainfall, and that erosion exhibited a gradient difference from the front to the rear edge. Model tests by Zhang Shuo et al. [8] indicated that short-duration intense rainfall mainly triggered shallow sliding, while long-duration rainfall was more likely to induce deep-seated flow slides. Zeng Changlu et al. and Guan Xiaodi et al. [9][10] further confirmed that there is a nonlinear relationship between rainfall intensity and the depth of the wetting front, with infiltration depth at the slope toe increasing by 40% under torrential rainfall conditions. By altering seepage boundary conditions, Bao Xiaohua et al. [11] revealed that infiltration from the upper part mainly induced shallow sliding, while infiltration from the bottom was more likely to result in overall sliding. Ma Beiqing et al. [12] discovered that when crack depth exceeded 60 cm, the safety factor of the slope would abruptly drop below 1.0. These experimental results were greatly enhanced by the application of advanced technologies such as three-dimensional laser scanning [7] and multi-physical field synchronous monitoring [13], which significantly improved the accuracy of data collection. With the development of computer technology, numerical simulation techniques have provided new insights into the infiltration analysis of slopes during rainfall. Liu Yin et al. [14] used FLAC3D simulations to find that a once-in-50-years rainfall event could reduce the maximum safe slope angle of a waste rock dump slope from 43° to 37°, revealing the detrimental effect of pore water pressure redistribution on shear strength. Wang Lei et al. [15], combining field tests with GeoStudio simulations, proved that the safety factor of a steep loess slope decreased by 58% after four days of continuous

Manuscript received April 17, 2025; revised June 18, 2025.

Jinggang Liu is a PhD candidate at Southwest Jiaotong University, Chengdu, Sichuan 610031 China (e-mail: 3069698751@qq.com).

Yaoxian Xie is a graduate student at Southwest Jiaotong University, Chengdu, Sichuan 610031 China (corresponding author to provide e-mail: 2590812150@qq.com).

Jiangtao Liu is an engineer at Shanghai Jiading Highway Construction and Development Co., Ltd., Shanghai 201800 China (e-mail: andy_liujt@163.com).

Xian Zhao is an engineer at Gansu Tieke Construction Engineering Consulting Co., Ltd., Lanzhou, Gansu 730000 China (e-mail: 515986205@qq.com).

Xianwen Huang is an engineer at Gansu Tieke Construction Engineering Consulting Co., Ltd., Lanzhou, Gansu 730000 China (e-mail: 515986205@qq.com).

Daheng Peng is an engineer at Gansu Tieke Construction Engineering Consulting Co., Ltd., Lanzhou, Gansu 730000 China (e-mail: 616672365@qq.com).

rainfall, validating the risk of shallow instability. Guo Yanbin et al. [16] used the GEO-SEEP/W module to demonstrate that reshaping an inverse S-shaped slope could enhance erosion resistance by homogenizing pore water pressure distribution. In terms of mechanism research, Du Zhongyuan et al. [17] used PLAXIS to reveal that high rainfall intensity accelerating the dissipation of negative pore water pressure could prompt the transition from shallow sliding to deep sliding. Lei Xiaoqin et al. [18] used a coupled model to quantitatively elucidate that permeability heterogeneity caused by fine particle migration was a key inducement of shallow instability. Bai Yajun et al. [19] improved the Mein-Larson infiltration model in combination with the strength reduction method, reducing the calculation error of the safety factor by 7.7% and significantly improving the reliability of numerical simulations.

This study focuses on typical high and steep loess slopes in Shanxi Province, employing a combination of indoor physical model tests and numerical simulations to systematically investigate the water-force coupling mechanism and instability evolution process of slopes under intense rainfall conditions. An artificial rainfall simulation system is used to precisely control rainfall intensity and duration, while pore water pressure sensors, soil pressure sensors, etc., are employed to obtain in real-time the evolution characteristics of the seepage field, deformation field, and failure patterns of the slope. Based on the GeoStudio2018 platform, a coupled calculation model integrating the SEEP/W module and SLOPE/W module is established to simulate the dynamic interaction between the unsaturated-saturated seepage field and stress field during rainfall infiltration. Experimental and simulation results indicate that there is a significant correlation between crack development and plastic zone expansion, with slope failure exhibiting progressive characteristics transitioning from shallow sliding to overall deep sliding. The synergistic response of the slope toe and slope crest serves as a precursor to overall instability. The study proposes instability warning indicators based on pore water pressure variation characteristics and displacement mutation points, providing a theoretical basis for the stability evaluation and disaster prevention and control of high and steep fill slopes.

II. Project Overview

This study takes the high and steep fill slope project of the third phase of the Xingbao Railway Storage and Transportation Facility in Baode County, Xinzhou City, Shanxi Province, as the experimental geological prototype. This project is located in a typical geological structural area of the Loess Plateau, characterized by typical loess hill and gully landforms. The micro-landform features in the study area are mainly loess ridges and deep gullies, with significant surface undulations and a relative height difference ranging from 10 to 30 m, locally reaching 80 m. The elevation ranges between +800 and +880 m. The surface vegetation cover in the area is relatively low, and the soil structure is loose with developed vertical joints, significant collapsibility, and complex engineering geological conditions.

The study area is located in a temperate continental semi-arid climate zone, characterized by distinct seasons, concentrated precipitation, dry weather, and significant diurnal temperature variations. The average annual temperature ranges from 10 to 12 ℃, and the average annual precipitation is between 230.8 and 458.38 mm. More than 60% of the rainfall occurs during the summer months (June to August), which is prone to short-duration intense rainfall events. According to measured data from the China Meteorological Administration, as shown in Figure 1, the precipitation characteristics of Xinzhou City in 2022 were characterized by an annual precipitation of 491.7 mm, a monthly extreme value of 196.3 mm, and a 24-hour extreme rainfall of 148.6 mm. Extreme rainfall during the rainy season (June to August) can easily induce slope instability, posing a high risk of landslide geological disasters. Therefore, this study employs indoor model tests and numerical simulations, based on the theory of unsaturated soil mechanics, to analyze the seepage-stress coupling mechanism and instability evolution laws of high and steep loess slopes under extreme rainfall conditions. The aim is to provide theoretical basis and data support for disaster prevention design of railway fill slopes on the Loess Plateau during the rainy season.

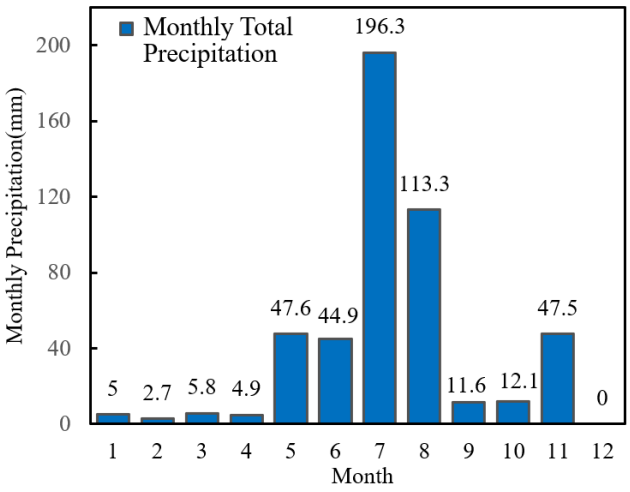

Fig.1. Monthly precipitation variation in Xinzhou City (2022)

III. Model Test Design

A. Resemblance

The problem of dominating the key physical quantities in a model test can be expressed as follows:

$$f=(l,u,w,q,d,k,t,c,\varphi,g,\rho,E,v,\sigma,\varepsilon)=0 \qquad (1)$$

where geometric length l, pore water pressure u, water content w, rainfall intensity q, displacement d, permeability coefficient k, time t, cohesion c, angle of internal friction φ, gravitational acceleration g, density ρ, modulus of elasticity E, Poisson's ratio v, stress σ, and strain ε are parameters. The similarity ratio for geometric length is determined as C_l = 100 and for gravitational acceleration as C_g = 1.

According to Buckingham's theorem (Buckingham, 1914; Buckingham, 1915), equation (1) can be expressed as follows to obtain the dimensionless parameters:

$$G(\pi_1,\pi_2,,\pi_3,\pi_4,\pi_5,\pi_6,\pi_7,\pi_8,\pi_9,\pi_{10},\pi_{11},\pi_{12})=0 \quad (2)$$

$$\pi_1=\frac{u}{lg\rho};\pi_2=w;\pi_3=\frac{q}{l^{\frac{1}{2}}g^{\frac{1}{2}}};\pi_4=\frac{d}{l};$$

$$\pi_5=\frac{k}{l^{\frac{1}{2}}g^{\frac{1}{2}}};\pi_6=\frac{t}{l^{\frac{1}{2}}g^{-\frac{1}{2}}};\pi_7=\frac{c}{lg\rho};\pi_8=\varphi;$$

$$\pi_9=\frac{E}{lg\rho};\pi_{10}=v;\pi_{11}=\frac{\sigma}{lg\rho};\pi_{12}=\varepsilon \quad (3)$$

The model material was loess taken from the site and compacted under density control, $C_\rho=C_E=C_c=C_k=1$, other parameter similarity ratios are $C_v=C_\varepsilon=C_\varphi=C_w=C_g=1$, $C_u=C_\sigma=C_d=C_l=100$, as commonly used in geotechnical model tests. For evaluating bearing capacity, the coefficient is defined as $C_q=\sqrt{C_l}\cdot\sqrt{C_g}=10$, and the time similarity ratio is given by $C_t=\frac{\sqrt{C_l}}{\sqrt{C_g}}=10$.

where C_l, C_u, C_w, C_q, C_d, C_k, C_t, C_c, C_φ, C_g, C_E, C_v, C_σ, and C_ε represent the geometric length l, pore water pressure u, water content w, rainfall intensity q, displacement d, infiltration coefficient k, time t, cohesion c, angle of internal friction φ, gravitational acceleration g, density ρ, modulus of elasticity E, Poisson's ratio v, and stress σ, respectively, of the prototype and model, Strain ε and other physical quantities of similarity ratio. According to the above theorem, a similarity link is established between the physical quantities of the prototype and the experimental model as shown in Table 1.

The test slope was designed according to a similarity ratio, with the following geometric parameters: slope height of 70 cm, platform width of 50 cm, base width of 100 cm, and slope angle of 63°. The entire slope was fixed to one side of the model box. The undisturbed soil used for the slope was obtained from a loess fill slope in Baode County, Xinzhou City, Shanxi Province. Laboratory tests were conducted to analyze the physical properties and hydraulic characteristics of this loess, with the data results detailed in Table 2. The collected loess samples were sieved through a 5 mm mesh screen, and the initial moisture content was controlled at 11%. The samples were then cured for 24 hours under plastic film cover before the test. Based on the 24-hour extreme rainfall record of 148.6 mm in Xinzhou City, the rainfall intensity for this study was set at 30 mm/h. Intermittent rainfall patterns were adopted for the test, with continuous rainfall from 10:00 to 18:00 over a period of 2 days, totaling 300 mm of rainfall. This was done specifically to ensure that the erosion and deformation observed in the model test closely resembled those under natural rainfall conditions.

TABEL 1
SIMILARITY RATIO BETWEEN MODEL AND PROTOTYPE

physical quantity	similarity ratio	physical quantity	similarity ratio
geometric length l	$C_l=100$	angle of internal friction φ	$C_\varphi=1$
pore water pressure u	$C_u=100$	gravitational acceleration g	$C_g=1$
moisture content w	$C_w=1$	densities ρ	$C_\rho=1$
intensity of rainfall q	$C_q=10$	modulus of elasticity E	$C_E=1$
displacement d	$C_d=100$	poisson's ratio v	$C_v=1$
permeability coefficient k	$C_k=1$	stresses σ	$C_\sigma=100$
time t	$C_t=10$	strains ε	$C_\varepsilon=1$
cohesive force c	$C_c=1$		

TABLE 2
PHYSICAL AND MECHANICAL PROPERTIES OF LOESS

materials	moisture content/%	maximum dry density/(g/cm^3)	liquid limit/%	plastic limit/%	cohesive force/kPa	angle/(°)	permeability coefficient/（m/s）
loess	11.4	1.91	24.2	14.9	10	29	4.7×10^{-6}

B. Test equipment

The dimensions of the model box are 100 cm × 400 cm × 800 cm (length × width × height). The top of the model box is open, and the four sides are made of transparent acrylic plates to facilitate the observation of soil changes. These plates have water-proofing capabilities, while the bottom consists of a steel plate supported by crossbeams. A grid of 10 × 10 cm² is drawn on the acrylic side plates to enable precise control during the filling process. To minimize boundary effects, Vaseline was applied to the acrylic side plates before filling.

The rainfall apparatus is a self-designed sprinkler-type device comprising atomizing sprinklers, a U-shaped iron frame, explosion-proof 912 tubing, and other components. To ensure uniform rainfall, systematic detection tests were conducted. A schematic of the test setup is shown in Figure 2. Three rain gauges are evenly placed along the bottom of the model box to monitor the rainfall distribution in real time.

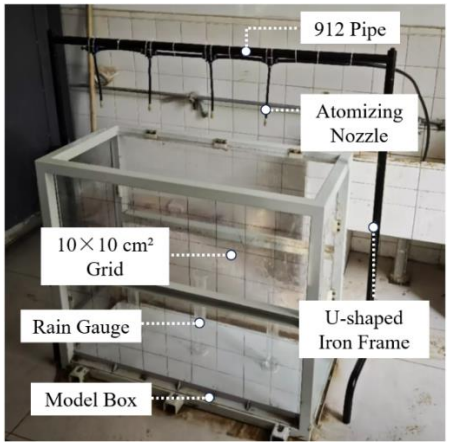

Fig.2. Experimental Setup for Rainfall Uniformity Testing

The periodic rainfall simulation scheme adopted in this experiment was implemented as follows: Firstly, the water supply system was activated to simulate rainfall for a continuous 100 minutes, followed by a 100-minute interval with the water supply turned off. This cyclic process was repeated until the cumulative experimental duration reached 600 minutes. The rainfall process curve is shown in Figure 3. At the set intensity of 30 mm/h, the measured spatial uniformity of rainfall reached 90%. This experimental design effectively simulated periodic rainfall conditions and verified the performance reliability of the rainfall simulation device.

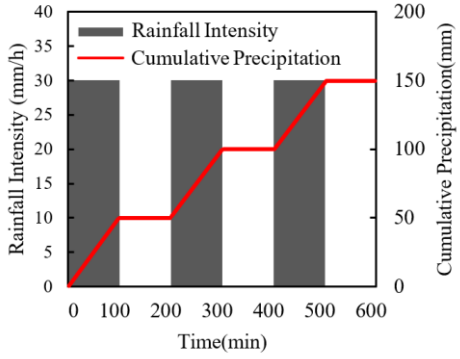

Fig.3. Rainfall Curve for Uniformity Testing

The monitoring system is shown in Figure 4 below, consisting of eight pore water pressure sensors (model: CYY2, with a diameter of 5 mm, a measurement range of 20 kPa, and an accuracy of 0.5%), eight micro soil pressure sensors (model: CS-TYJ1000, with a diameter of 20 mm and a measurement range of 1000 kPa), 21 golf tee markers (5 mm in diameter), and a DM-YB1820 dynamic and static strain testing system. All sensors were calibrated before the experiment, and during the experiment, pore water pressure and soil pressure were measured every minute using the DM-YB1820 dynamic and static strain testing system.

（a）Pore water pressure sensors

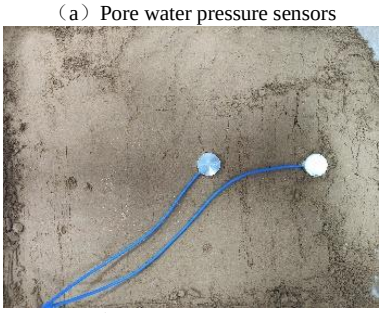

（b）Earth pressure sensors

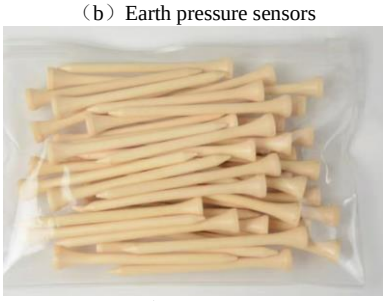

（c）Golf spikes

（d）20-channel strain test system

Fig.4. Schematic Diagram of the Monitoring System

C. Model preparation

During the experiment, a layered filling technique was employed to construct the 63° loess slope model. Each filling layer was strictly controlled at a thickness of 10 cm and evenly laid in the model box after precise weighing. During filling, a scraper was first used for initial leveling, followed by progressive compaction using a handheld compacting instrument along an "S"-shaped trajectory longitudinally across the model box, until the soil surface

reached the preset layered datum line on the acrylic plate. technique ensured the structural homogeneity and geometric accuracy of the steep slope fill body through three key processes: metering and filling, layered compaction, and elevation calibration. To maintain the overall uniformity of the model, the compacting force and operational path for each soil layer were required to be consistent. Additionally, the density and moisture content of the soil were strictly controlled according to the parameters in Table 2. After each layer was filled, a cutting ring (with a diameter of 8 cm and a height of 4.5 cm) was used to take samples to measure the soil density. If the measured density was too low, additional compaction was applied to that layer; if the density exceeded the standard range, the layer was removed and refilled to ensure the scientific validity and reliability of the experimental data.

The layout of the sensors is shown in Figure 5. To monitor the internal response characteristics of the slope, eight equally spaced monitoring sections were arranged at depths of 10 cm and 30 cm parallel to the slope surface. Each monitoring section was equipped with a dual-parameter sensing system, including one pore water pressure sensor and one soil pressure sensor, to enable synchronous multi-parameter monitoring of the soil-water coupling effect. To accurately quantify the displacement changes of the fill slope during the experiment, golf tee markers were used as reference points. The ends of these markers were trimmed and embedded into the compacted loess, ensuring their positions corresponded to a total of 21 grid nodes close to the slope surface. This arrangement enabled effective monitoring and data collection of the displacement field. The layout of the golf tee markers is shown in Figure 6.

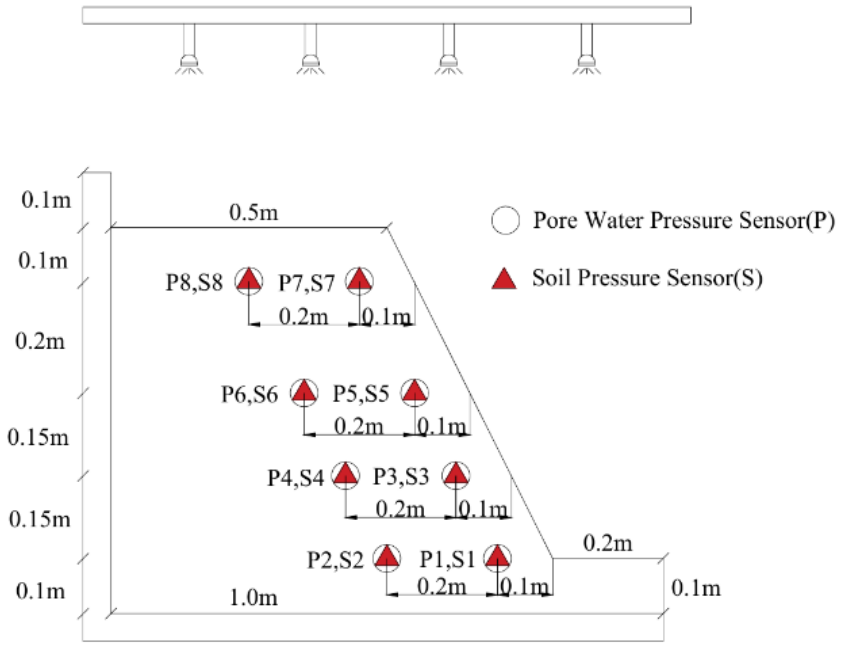

Fig.5. Schematic of Sensor Layout in the Experiment

Fig.6. Layout of Golf Ball Pins

IV. Test Results and Analysis

A. Analysis of soil pressure changes

Based on the soil pressure monitoring data shown in Figure 7, under continuous rainfall conditions, the spatio-temporal distribution of soil pressure within the slope exhibits significant non-uniformity. At the initial stage of monitoring, the soil pressure at all measurement points was 0 kPa. After the onset of rainfall, the soil pressure generally showed an upward trend, indicating that rainwater infiltration led to an increase in soil saturation and self-weight. There were considerable differences in the response time and magnitude of change among different measurement points. Shallow measurement points S7 and S8 reached peak soil pressures of 1.1 kPa and 0.8 kPa, respectively, approximately 80 minutes after the start of rainfall, followed by an inflection point and a gradual decrease. This was related to the concentrated seepage of rainfall due to crack development at the slope crest. The formation of cracks reduced soil saturation, triggering the release of self-weight stress and attenuation of horizontal soil pressure. When rainfall continued for approximately 790 minutes, large-scale instability occurred in the shallow soil layer due to the interconnection of cracks, and the soil pressure began to drop sharply to -1.5 kPa and stabilized, indicating that the soil had entered the plastic failure stage at this point. Similar phenomena were observed at medium-depth measurement points S5 and S6, but their inflection points lagged behind to about 600 minutes, with peak soil pressures of 2.8 kPa and 2.2 kPa, respectively, followed by decreases to 0.2 kPa and -0.6 kPa, respectively. This reflected the coupling effect of crack propagation depth and permeation lag effect. When shallow cracks developed, the deep soil was still in the stage of continuous water infiltration. The soil pressure began to decrease only after the cracks penetrated to the corresponding depth.

The changes in soil pressure at measurement points S1 and S3 at the slope toe further revealed the priority of local failure. Their initial growth rates were higher, reaching peak values of 1.5 kPa and 1 kPa, respectively, at about 380 minutes after the start of rainfall. However, due to the impact of runoff erosion and gully development, the downward trend occurred earlier than at other measurement points. At the end of rainfall, the S1 sensor failed due to gully erosion, causing the soil pressure to rapidly return to zero. This phenomenon directly verified the characteristic of the slope toe as a stress concentration area where failure occurs preferentially. In contrast, the soil pressure at deep measurement points S2 and S4 (with greater burial depths) rose slowly after about 190 minutes of rainfall and reached peak values of 1.2 kPa and 1.5 kPa, respectively, at about 800 minutes of rainfall, without significant inflection points. This indicated that this area did not experience significant seepage loss or structural damage, and water continuously increased the effective stress of the soil through matrix infiltration. This was because the shallow soil was dominated by fissure seepage, while the dynamics of deep soil were controlled by matrix infiltration.

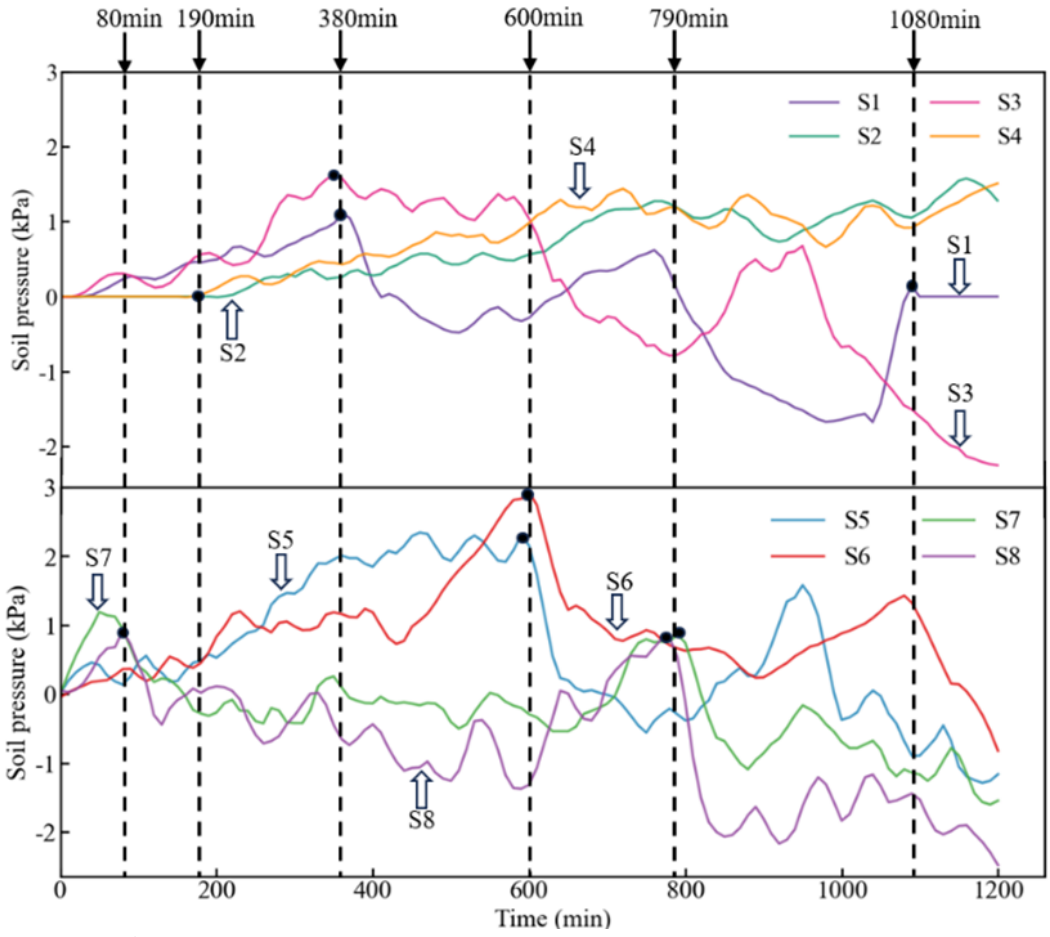

Fig.7. Time History Curve of Soil Pressure

Based on the comprehensive monitoring data obtained from various measurement points across the slope surface and subsurface, it can be systematically inferred that the failure process of the high-steep slope under rainfall infiltration follows a progressive and sequential pattern characterized by the transition from the slope toe to the slope crest and ultimately to the slope middle. Specifically, the initial signs of localized instability manifest at the slope toe, primarily triggered by the concentration of shear stress and the continuous action of surface runoff erosion. These factors significantly reduce the shear strength of the shallow soil layer at the toe, initiating localized deformation and stress redistribution.

Concurrently, tension cracks are observed to develop at the slope crest under tensile stress, forming potential preferential flow paths that facilitate rapid infiltration of rainwater. These preferential pathways play a critical role in accelerating the attenuation of matric suction and enhancing local saturation, thereby weakening the mechanical integrity of the crest zone. In contrast, the central region of the slope, due to its relatively longer seepage path and delayed crack propagation, exhibits signs of failure at a later stage, completing the full progression of the failure mechanism.

The evolution of this failure mode is visually confirmed in the frontal deformation profile of the test slope, as illustrated in Figure 8. The overall deformation and failure characteristics exhibit high consistency with the coupled hydro-mechanical response of unsaturated soils subjected to rainfall infiltration. The process of water infiltration leads to a substantial reduction in soil matric suction, while simultaneously increasing the self-weight of the soil mass due to elevated moisture content. These changes intensify the internal stress state of the slope. The formation and expansion of cracks significantly modify the spatial distribution of the infiltration field within the slope body, thereby inducing complex patterns of stress redistribution and strain localization. This internal reorganization ultimately leads to progressive slope destabilization and collapse. The findings also highlight that the inflection point observed in the shallow soil pressure curve can act as a highly sensitive early warning indicator for the critical state of crack interconnectivity. Moreover, the observed synergistic deformation response between the slope toe and crest regions serves as a reliable precursor signal for the onset of global slope instability.

（a）Initial state of the slope

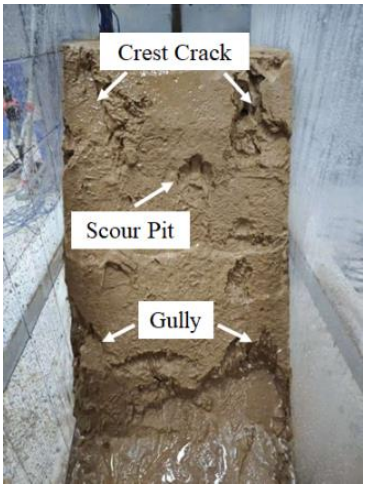

（b）Stages of crack development at the foot and top of Slopes

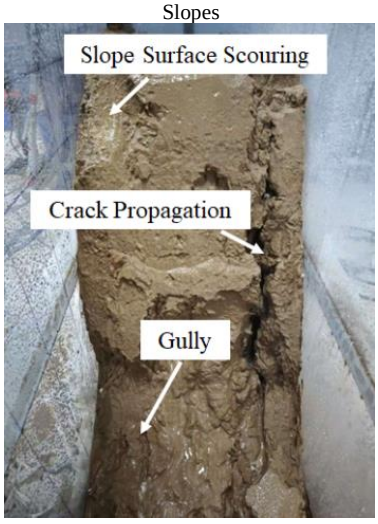

（c）Crack penetration and slope failure phase

Fig.8. Evolution Process of Slope Failure

b. Pore water pressure change analysis

The time-history variations of pore water pressure recorded during the rainfall infiltration process are illustrated in Figure 9. At the onset of rainfall, the pore water pressure at monitoring points P1, P3, P5, P7, and P8 exhibited a rapid increase, indicating an immediate hydrological response of the slope surface and shallow subsurface. Notably, around the 80-minute mark, local extreme values were recorded at key locations: 1.10 kPa at the slope toe (P1) and 2.75 kPa at the slope crest (P7). In contrast, the changes in pore water pressure at mid-slope monitoring points P2, P4, and P6 were relatively subdued, suggesting a delayed hydrological response.

This spatial variation is primarily attributed to the dual characteristics of the wetting front propagation during the early stage of rainfall. Horizontally, the wetting front spreads along the crest zone due to surface infiltration and lateral flow, while vertically it penetrates downward along the slope profile. This coupled infiltration pattern leads to a more immediate response in the slope toe and crest regions, which are more vulnerable to water ingress, whereas the mid-slope zone exhibits a lagged response due to its greater seepage path length and the presence of overlying unsaturated soil layers.

As erosion-induced cracks developed at the slope toe and tensile cracks formed at the slope crest, a sharp drop in pore

water pressure occurred between 80 and 200 minutes at points P1 and P7. This drop was caused by the abrupt alteration of the local hydraulic gradient, as shallow cracks created preferential flow paths that allowed rainwater to bypass the matrix flow and either escape rapidly or infiltrate deeper into the slope. Consequently, this triggered a sudden release of pore water pressure, reflecting the onset of structural reconfiguration within the slope mass.

Following this initial drop, pore water pressure at P7 and P8 entered a relatively stable phase, whereas a slight upward trend began to emerge at mid-slope monitoring points P3, P4, P5, and P6. The slower rise at these locations can be attributed to the extended infiltration time, the protective effect of the upper soil layers, and inherent soil heterogeneity, which together retard the advancement of the wetting front. As rainfall persisted, during the 400–600 minute period, a secondary and more pronounced rise in pore water pressure was observed at slope toe and crest points P1 and P7, reaching new peak values of 1.38 kPa and 2.85 kPa, respectively. This indicates that the saturation zone had expanded into deeper soil layers, driving a significant increase in positive pore pressure and causing the dominant seepage paths to shift toward the slope surface. This process resulted in a steepened hydraulic gradient, particularly in the slope shoulder and toe zones, enhancing the slope's vulnerability to failure.

Subsequently, after 900 minutes of continuous rainfall, another abrupt drop in pore water pressure was recorded at P1 and P7. This second drop can be attributed to localized structural failures in the slope, including deformation and displacement at the shoulder and toe, as well as the mechanical breakdown of soil aggregates under sustained wetting. These failures facilitated the rapid dissipation of pore water pressure through newly formed preferential flow channels.

While the trends in pore water pressure variation at different monitoring points displayed a consistent general pattern, they exhibited notable differences in terms of response timing, amplitude of fluctuation, and stage of hydromechanical evolution. The entire pressure evolution process demonstrated a distinct “double-peak and double-drop” characteristic, which vividly reflects the complex interaction among rainfall infiltration, crack initiation and propagation, temporal changes in hydraulic conductivity, and the structural deformation response of the slope. These comprehensive findings offer critical insights into the underlying pore pressure dynamics that govern rainfall-induced slope instability and provide valuable reference information for the development of early warning systems and quantitative hazard assessment strategies.

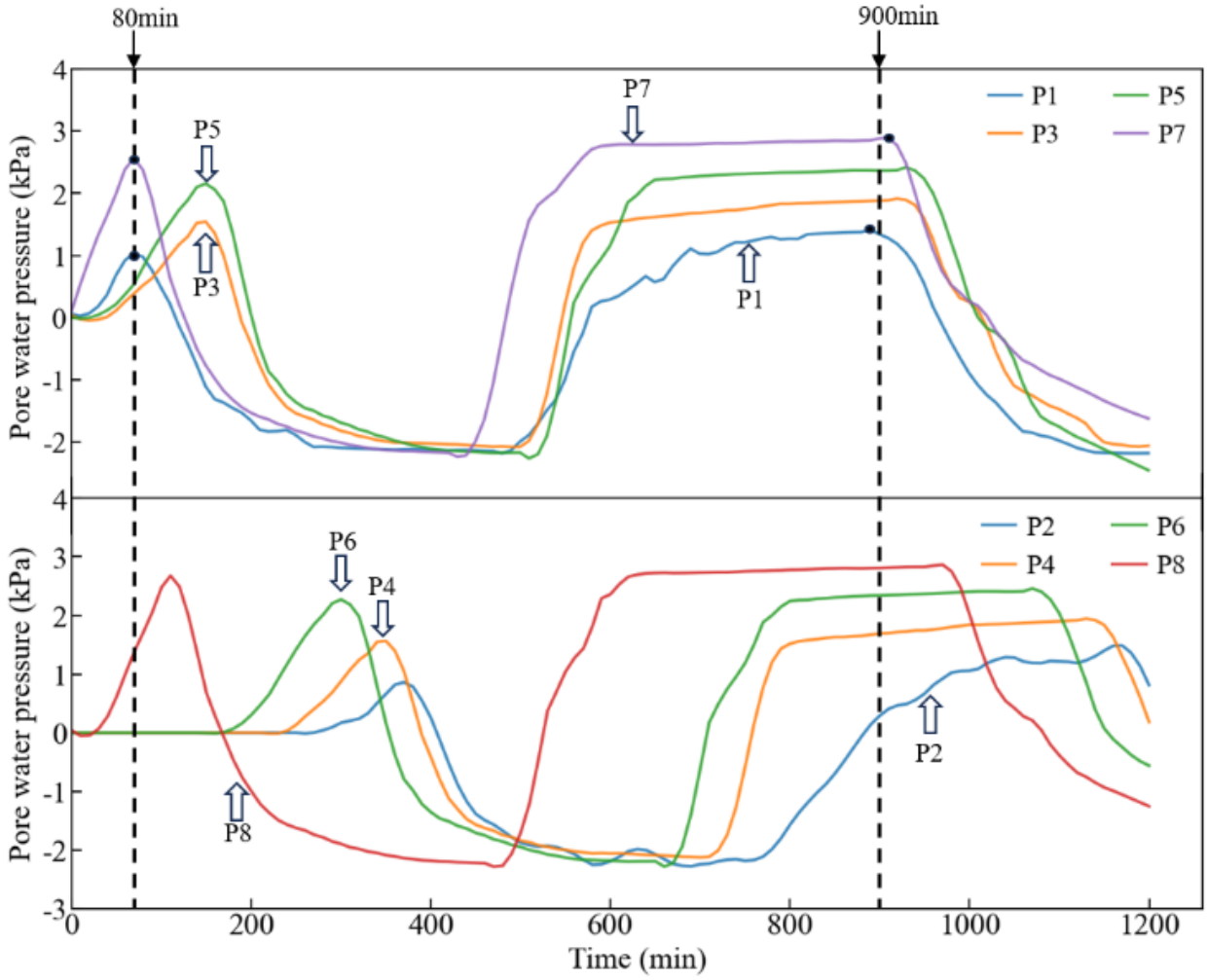

Fig.9. Time History Curve of Pore Water Pressure

The numerical simulation utilized the Seep/w module within the GeoStudio software suite to evaluate the hydrological response of the experimental slope under an intense rainfall condition of 30 mm/h. The established finite element mesh and corresponding boundary conditions are illustrated in Figure 10. The model represents a physical slope with a length of 1.0 m and a height of 0.7 m. The bottom and left boundaries were designated as impermeable to simulate underlying bedrock conditions commonly encountered in field settings; thus, both were assigned as zero unit flow (no-flow) boundaries to reflect realistic hydrogeological constraints. Given that the groundwater table in typical field scenarios is positioned at a much deeper elevation, its influence on the seepage process was omitted from the numerical analysis.

Since the applied rainfall intensity substantially exceeded the saturated hydraulic conductivity of the slope soil, the rainfall boundary was modeled using a pressure head condition rather than a flux boundary. A constant pressure head of 0.15 m was imposed to reflect the effective ponding depth and ensure the establishment of saturated flow at the soil surface during the early stages of infiltration. In order to account for the dynamic transition of soil from an unsaturated to a saturated state during rainfall infiltration, the simulation was carried out based on the saturated–unsaturated seepage theoretical framework. The Van Genuchten model was employed to describe the constitutive relationship between soil volumetric water content and effective permeability. Relevant soil hydraulic parameters were obtained and optimized using the built-in estimation and calibration functions provided by the GeoStudio software, ensuring consistency with the soil's physical behavior under transient flow conditions.

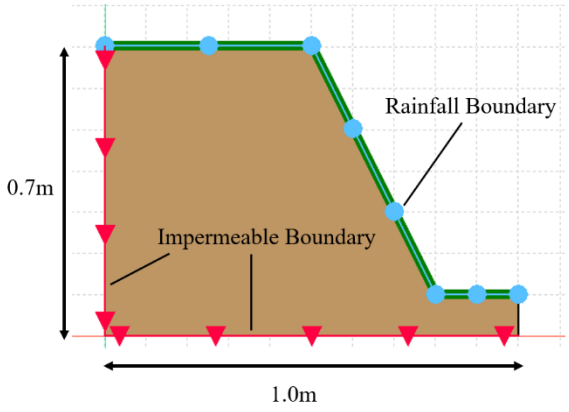

Fig.10. Finite element model for rainfall infiltration analysis

The numerical analysis results depicting the temporal evolution of pore water pressure, obtained using the GeoStudio software platform, are illustrated in Figure 11. In general, the simulated curves at various monitoring points exhibited a typical pattern characterized by an initial sharp rise in pore water pressure followed by a gradual decline. This trend is consistent with the expected hydromechanical behavior of unsaturated soil subjected to sustained rainfall infiltration. Nevertheless, it is noteworthy that the numerical simulation was unable to capture the abrupt drops in pore water pressure observed during physical testing, which are primarily attributed to the development and propagation of structural cracks within the slope body. This discrepancy underscores a key limitation of the numerical modeling framework employed in this study, namely the lack of incorporation of structural discontinuities or fracture mechanics. The influence of this limitation was particularly evident at monitoring point P7, where two distinct pore pressure drops were recorded in the experimental data, whereas the simulated curve failed to reflect any such sudden transitions.

During the simulation under a constant rainfall intensity of 30 mm/h, the pore water pressure at all instrumented locations followed an evolution pattern best described as “a rapid initial increase followed by gradual stabilization.” This behavior reflects the dynamic interaction between rainfall infiltration, soil permeability, and the redistribution of pore water pressure within the slope mass. When comparing the numerical results to the experimental observations, it is apparent that the simulated response was more immediate and intensified. This deviation arises due to differences in sensor dynamics: in the physical model tests, the pore pressure sensors required a certain duration for water to permeate the protective gravel layer and fully engage the sensing membrane, thereby introducing a lag in measured response. This lag is not present in the numerical model, which assumes instantaneous hydraulic continuity, thus producing faster pressure fluctuations. Both the numerical simulations and the physical model tests consistently demonstrated that the magnitude of pore pressure variation was significantly greater at upper monitoring points compared to those positioned at lower elevations. This spatial disparity highlights the heterogeneity of infiltration paths and the directional propagation of the wetting front. Specifically, rainfall infiltration initially impacts the upper slope regions where the soil is more directly exposed, leading to a more rapid saturation process and a steeper pressure gradient. In contrast, the lower slope zones experience more gradual pressure changes due to the longer flow paths, reduced permeability, and vertical heterogeneity of the soil medium. These findings collectively provide valuable insight into the spatial and temporal characteristics of pore water pressure distribution during rainfall infiltration in unsaturated slopes. Furthermore, they reveal the inherent limitations of conventional numerical simulation techniques, particularly when localized failure mechanisms such as tensile cracking or hydraulic fracturing are not considered.

The inability of the model to replicate observed pressure drops indicates that the exclusion of fracture mechanics can lead to oversimplified and potentially misleading interpretations of slope behavior under rainfall. By critically comparing the numerical and experimental results, the study reinforces the significance of seepage–deformation coupling and crack-induced permeability changes in controlling slope stability. It is therefore strongly recommended that future research efforts adopt advanced numerical modeling approaches capable of capturing crack initiation, propagation, and their consequent impacts on the evolution of hydraulic conductivity within slope materials. These improvements will significantly enhance the accuracy of predicting and evaluating complex failure behaviors across diverse slope systems subjected to sustained and long-duration rainfall infiltration.

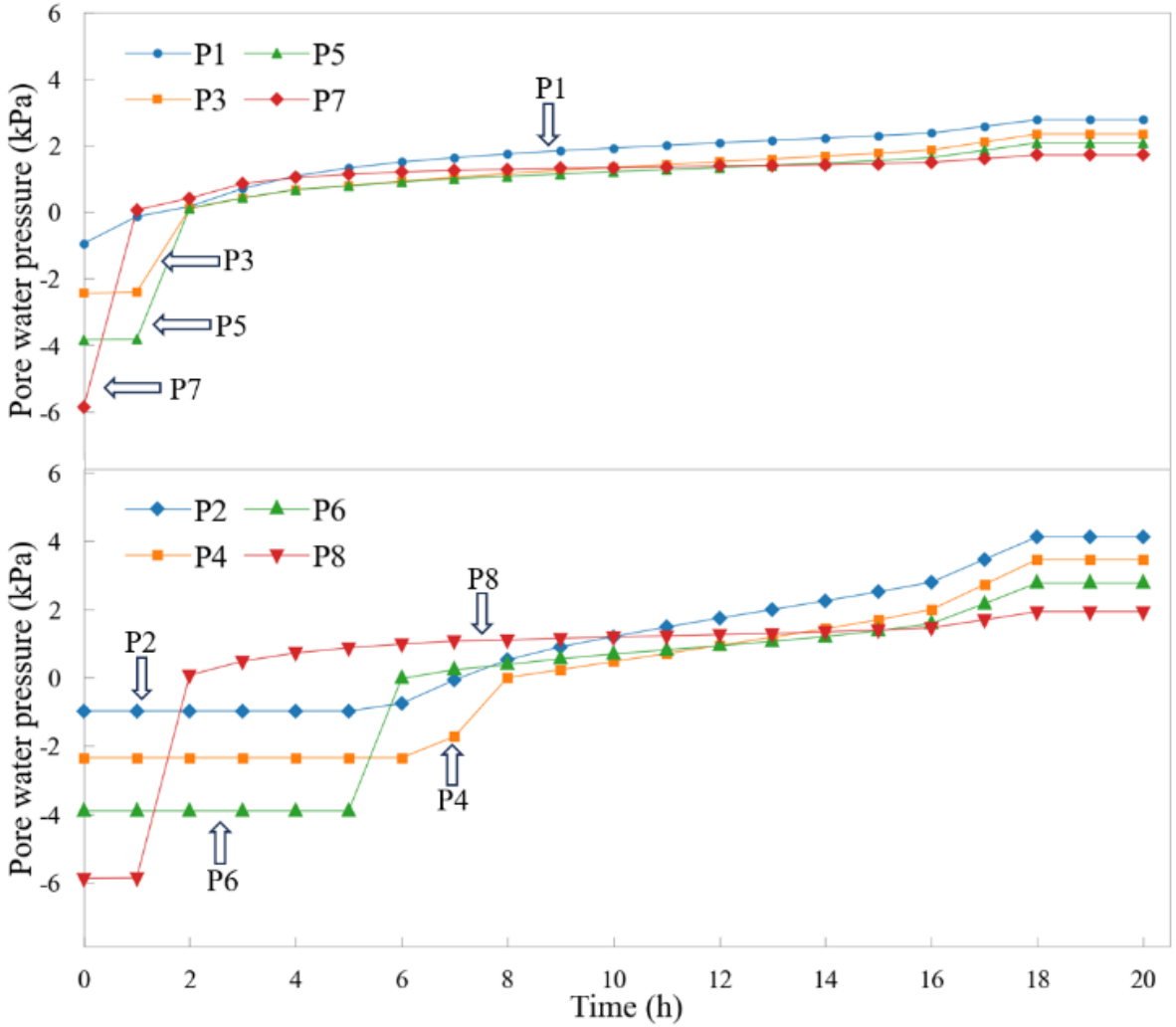

Fig.11. Numerical Simulation Curve of Pore Water Pressure

c. Slope deformation analysis

Displacement is one of the most intuitive external manifestations in the evolution process of slope instability. In this study, golf tee marking method was utilized to monitor the displacement evolution of soil at different depths within a fill slope under rainfall. Due to the low visibility of the tees inside the slope, Figure 12(a) has undergone computer image processing to enhance the clarity of the marking points. Experimental observations revealed that the slope soil exhibited typical layered deformation characteristics under rainfall infiltration, with the sixth soil layer showing the most significant displacement response, featuring a vertical displacement of 4.2 cm and a horizontal displacement of 2.1 cm. The displacement field exhibited a gradient attenuation distribution along the depth direction, which is attributed to the compaction effect under the action of soil self-weight stress field: As the burial depth increases, the degree of soil compaction caused by overlying loads increases, effectively constraining deep deformations through micromechanical mechanisms such as particle rearrangement and contact force chain reconstruction. Additionally, due to erosion damage at the slope toe, the tee closest to it in the first layer has been eroded and detached, further indicating the impact of slope toe erosion on slope stability.

The angle α between the displacement direction (AB) of the golf tee and the horizontal baseline (AC) gradually increases to 90° as depth increases, indicating that the soil undergoes displacement in both vertical and horizontal directions. However, as depth increases, the horizontal displacement gradually diminishes until it disappears. This trend further verifies the constraining effect of the compaction of overlying soil layers on the displacement of deeper soil. The horizontal displacement of the slope decreases to zero approximately 30 cm from the slope toe, suggesting that the slope slip range is within 0.3 m and mainly concentrated in the upper loose fill area, forming a shallow curved sliding surface.

The numerical analysis results of slope stability based on GeoStudio software are shown in Figure 12(b). The analysis indicates that the predicted sliding surface aligns well with the post-experimental deformation pattern of the slope, particularly consistent with the height of the sliding surface in the middle of the tested slope. The sliding of the upper fill soil results in the formation of a collapse scarp at the slope toe, while tensile cracks at the slope crest accelerate shallow water migration, further promoting the development of the sliding surface. The dominant factors contributing to the formation of the slip surface include the accumulation of pore water pressure, the permeability characteristics of weak layer interfaces, and the water conduction effect of cracks. These factors act together to gradually form and expand the

slip surface towards the interior of the slope, ultimately inducing slope instability. The sliding characteristics on the side of the tested slope are not obvious, and the sliding effect differs from that in the central region due to the incomplete elimination of the wall effect. The safety factor of the potential sliding surface of the high and steep loess slope is only 0.705, which is attributed to the insufficient natural stability caused by the slope's geometric characteristics and the further exacerbated risk of slope instability due to the loss of matrix suction and the action of seepage forces induced by extreme rainfall.

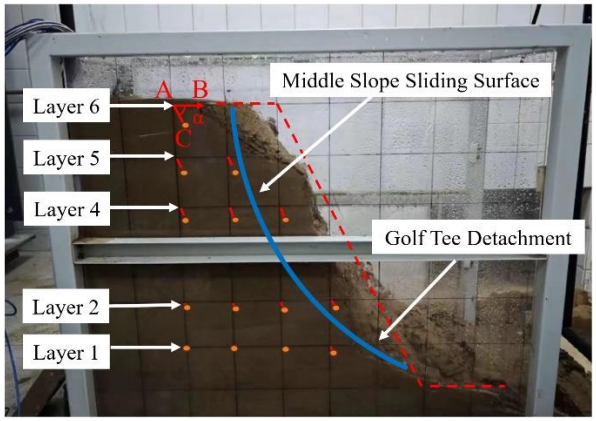

（a）Plot of slope displacement changes

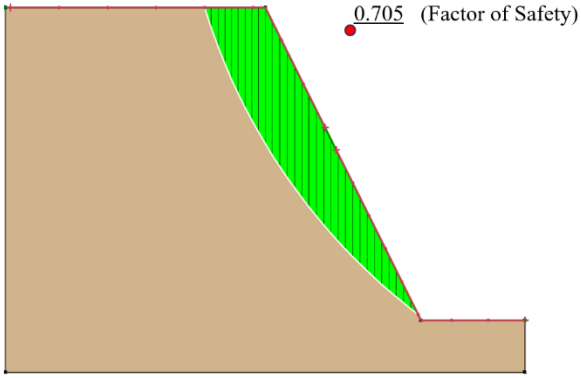

（b）Map of slip surface prediction results

Fig.12. Comparison of Slope Displacement and Predicted Slip Surface

V. Conclusions

(1) The failure modes of slopes induced by rainfall exhibit phased characteristics. The process of slope failure can be divided into four stages: rainfall infiltration, pore water pressure rise, shear strength reduction, and instability failure. During the initial stage of rainfall infiltration, the wetting front rapidly expands along the slope surface, forming dual seepage paths, which leads to the development of cracks at the slope crest and the concentration of shear stress at the slope toe. As pore water pressure increases, the strength of the shallow soil layer of the slope gradually decreases, entering the stage of instability and failure.

(2) The evolution of pore water pressure demonstrates a prominent "double-peak and double-drop" characteristic. Both experimental monitoring and numerical simulation results indicate that this dynamic process can be divided into four distinct stages: initially, pore water pressure rapidly rises to the first peak; then, due to the formation of cracks within the slope, it suddenly drops, forming the first trough; next, it rises again to a second peak; finally, with further crack penetration and expansion, it sharply drops again and gradually stabilizes. Notably, the variation amplitude of pore water pressure at the slope crest and toe is significantly greater than at the mid-slope, with the fastest decay rate observed at the toe. This phenomenon may primarily result from stress concentration and runoff erosion at the slope toe (evidenced by early soil pressure peaks at S1/S3 in Fig 7 and sensor failure due to gully erosion), while crack penetration at the slope crest further accelerates the pore pressure release. Their combined synergistic effect constitutes a critical precursor to rainfall-induced slope failure. To effectively reduce such risks, engineering measures such as constructing drainage channels are recommended to promptly remove the retained water in cracks and significantly enhance the overall slope stability.

(3) The displacement distribution of the slope gradually decreases from shallow to deep, with a limited slip range. Experimental results show that the displacement of the sixth soil layer is the largest, with a vertical displacement of 4.2 cm and a horizontal displacement of approximately 1.1 cm. The slip range is concentrated in the upper loose fill area, and the horizontal displacement gradually decreases to zero at a distance of 30 cm from the slope toe, forming a shallow curved sliding surface within 0.3 m. The displacement trajectories of the golf tees reveal the progressive sliding characteristics of the slope body, which are basically consistent with the prediction results of numerical simulations. Numerical simulations based on GeoStudio software effectively reproduce the dynamic changes in the seepage field, stress field, and displacement field of the slope under rainfall. The predicted sliding surface aligns well with the post-experimental deformation of the slope, but the sliding characteristics on the slope side are not obvious due to the wall effect. It is necessary to further optimize the model boundary conditions to improve experimental accuracy. With a safety factor of 0.705, it is recommended to adopt reinforcement measures such as reinforced soil in engineering practice to effectively enhance the overall stability and anti-sliding capacity of the slope, thereby reducing the probability of landslides.

References

[1] MENG Zhenjiang, CAO Yidi, KANG Chenyun, et al. Simulation of the Initiation Mechanism of Loess Landslide Promoted by Rainfall[J]. Journal of Earth Sciences and Environment,2023,45(3):474-484.

[2] PENG J, SUN P, IGWE O. Loess caves, a special kind of geo-hazard on loess plateau, northwestern China[J]. Engineering Geology,2018,236:79-88.

[3] Jin Zhao, Peng Jianbing, Zhuang Jianqi, et al. Gully erosion and expansion mechanisms in loess tablelands and the scientific basis of gully consolidation and tableland protection[J]. Science China Earth Sciences,66(4):821–839.

[4] YU Daijin, HUANG Qiangbing, KANG Xiaosen, et al. A model test study of the interface seepage and failure mechanism of loess-filled slope[J]. Hydrogeology & Engineering Geology,2022,49(5):119-128

[5] WANG Chenghai, ZHANG Shengning, ZHANG Feimin,et al. On the increase of precipitation in the Northwestern China under the global warming[J].Advances in Earth Science,2021,36(9):980-989.

[6] HAN Jiaming, DONG Zhao, SU Sanqing, et al. Analytical solution of rainfall infiltration in homogeneous unsaturated slope and its application in loess slope[J]. Rock and Soil Mechanics,2023,44(01):241-250.

[7] ZHU Jiandong, WU Lizhou, LI Shaohong, et al. Laboratory Experiment of Rainfall-induced Erosion on Loess Slopes Under Two Rainfall Patterns[J]. Journal of Soil and Water Conservation,2019,33(06):92-98.

[8] ZHANG Shuo, PEI Xiangjun, HUANG Runqiu, et al. Model Test on Seepage Characteristics and Deformation Failure Modes of Loess Fill Slope Under Rainfall[J]. China Journal of Highway and Transport,2019,32(09):32-41+50.
[9] ZENG Changlu, LI Rongjian, GUAN Xiaodi, et al. Experimental study on rainfall infiltration characteristics of loess slopes under different rainfall intensities[J]. Chinese Journal of Geotechnical Engineering,2020,42(S1):111-115.
[10] GUAN Xiaodi, LI Rongjian, PAN Junyi, et al. Testing and comparison of heavy rainfall infiltration of loess slope at different slope ratios[J]. Journal of Xi′an University of Technology,2021,37(02):286-294.
[11] BAO Xiaohua, LIAO Zhiguang, XU Changjie, et al. Model test study of the failure of silty sand slope under different seepage boundary conditions[J]. Rock and Soil Mechanics,2019,40(10):3789-3796.
[12] MA Beiqing, DU Yupeng, WANG Huaixing, et al. Experimental Study on Stability of Loess Slope Stability Under Continuous Rainfall[J]. Journal of Soil and Water Conservation,2021,35(05):50-56.
[13] LIANG Jixing, LIU Lei, XU Jiye, et al. Rainfall Model Test and Numerical Analysis of Seepage Characteristics of Dump Slope[J]. Mining Research and Development,2024,44(09):94-102.
[14] LIU Yin, WANG Yuanlai, SHI XiuZhi, et al. Slope Stability Analysis for Waste Rock Dump Based on Consideration of Rainfall[J]. Mining and Metallurgical Engineering,2022,42(05):26-29.
[15] WANG Lei, LI Rongjian, LIU Junding, et al. Stability evaluation and cracking research of steep loess slope under continuous rainfall[J]. Hydro Science and Engineering,2022(4):77-86.(in Chinese).
[16] GUO Yanbin, ZHANG Chuanwei, TIAN Guang, et al. Research on seepage and pore water pressure characteristics of internal dump near-natural remodeling[J]. Safety in Coal Mines,2023,54(2):161-165.
[17] Du Zhongyuan,Ge Xinsheng,Tong Fei. Stability analysis of high slope under different rainfall conditions[J]. Science Technology and Engineering,2021,21(30):13039-13045.
[18] Lei Xiaoqin, Liu Enlong, He Siming,et al.Modelling of coupled process of rainfall infiltration and internal erosion within unsaturated deposited soil slopes[J]. Advanced Engineering Sciences,2021,53(2):28–37..
[19] BAI Yajun, REN Jianmin, TIAN Min, et al. Improved Mein-Larson rainfall infiltration model-based stability analysis of loess slope[J]. Water Resources and Hydropower Engineering,2023,54(4):131-139.